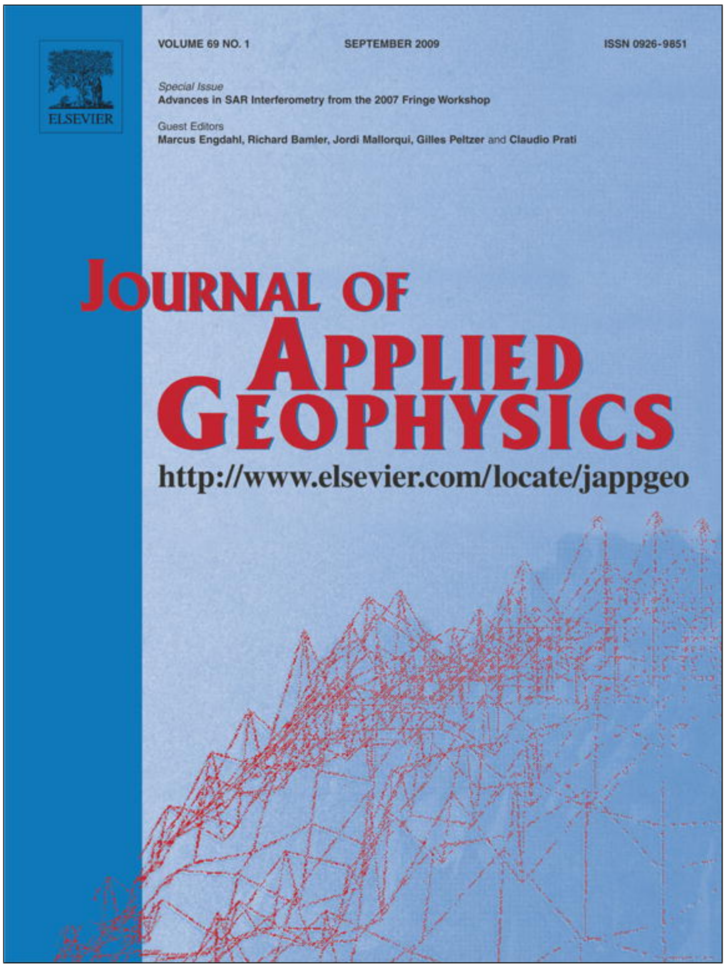
VOLUME 69 NO. 1
SEPTEMBER 2009
ISSN 0926-9851
Special Issue
Advances in SAR Interferometry from the 2007 Fringe Workshop
Guest Editors
Marcus Engdahl, Richard Bamler, Jordi Mallorqui, Gilles Peltzer and Claudio Prati
ELSEVIER
JOURNAL OF APPLIED GEOPHYSICS
http://www.elsevier.com/locate/jappgeo

Journal of Applied Geophysics 69 (2009) 1–15

Contents lists available at ScienceDirect

Journal of Applied Geophysics

journal homepage: www.elsevier.com/locate/jappgeo

Time series analysis of Mexico City subsidence constrained by radar interferometry

Penélope López-Quiroz [a,b,*,1], Marie-Pierre Doin [a], Florence Tupin [b], Pierre Briole [a], Jean-Marie Nicolas [b]

[a] Laboratoire de Geologie, École Normale Supérieure, CNRS UMR 8538, Paris, France
[b] Institut TELECOM, TELECOM ParisTech, LTCI CNRS UMR 5141, 75013 Paris, France

ARTICLE INFO

Article history:
Received 21 April 2008
Accepted 8 February 2009

Keywords:
InSAR
Interferogram unwrapping
Tropospheric corrections
Land subsidence
Time series
Mexico City

ABSTRACT

In Mexico City, subsidence rates reach up to 40 cm/yr mainly due to soil compaction led by the over exploitation of the Mexico Basin aquifer. In this paper, we map the spatial and temporal patterns of the Mexico City subsidence by differential radar interferometry, using 38 ENVISAT images acquired between end of 2002 and beginning of 2007. We present the severe interferogram unwrapping problems partly due to the coherence loss but mostly due to the high fringe rates. These difficulties are overcome by designing a new methodology that helps the unwrapping step. Our approach is based on the fact that the deformation shape is stable for similar time intervals during the studied period. As a result, a stack of the five best interferograms can be used to compute an average deformation rate for a fixed time interval. Before unwrapping, the number of fringes is then decreased in wrapped interferograms using a scaled version of the stack together with the estimation of the atmospheric phase contribution related with the troposphere vertical stratification. The residual phase, containing less fringes, is more easily unwrapped than the original interferogram. The unwrapping procedure is applied in three iterative steps. The 71 small baseline unwrapped interferograms are inverted to obtain increments of radar propagation delays between the 38 acquisition dates. Based on the redundancy of the interferometric data base, we quantify the unwrapping errors and show that they are strongly decreased by iterations in the unwrapping process. A map of the RMS interferometric system misclosure allows to define the unwrapping reliability for each pixel. Finally, we present a new algorithm for time series analysis that differs from classical SVD decomposition and is best suited to the present data base. Accurate deformation time series are then derived over the metropolitan area of the city with a spatial resolution of 30×30 m.

1. Introduction

Mexico City, one of the most populated cities in the world, records among the largest subsidence rates ever measured. Subsidence rates reach up to 40 cm/yr (Strozzi et al., 2003; Cabral-Cano et al., 2006) in some areas of the city with locally large subsidence gradients affecting the whole urban structure. Mexico City is located in the southern part of the Mexico Valley, an endoreic basin surrounded by mountains, formerly filled by several lakes until the Spanish conquest (see Fig. 1). Those lakes were dried by Spanish conquerors and the city was built on the former lake bottom.

The simplified hydrogeological structure of the Mexico Valley includes a main hydrogeological unit called the quaternary alluvial unit (see Fig. 1) or aquifer, reached by the extraction wells located at a maximum depth of 300 m. This layer has a maximum thickness of approximately 800 m and is partially covered by 30 to 300 m thick quaternary lacustrine deposits (See Fig. 1), forming the aquitard (Carrera-Hernández and Gaskin, 2007). The aquitard layer plays a crucial role in the subsidence process due to the very high compressibility of its clay and silt sediments. The aquifer provides 70% of the Mexico City population water consumption (Tortajada, 2006). Its over exploitation causes a gradual potentiometric draw-down (~70 m in Ecatepec between 1975 and 2002, Carrera-Hernández and Gaskin, 2007), reducing the interstitial water pressure at the base of the aquitard. Diffusion of the negative pore pressure anomaly within the low permeability aquitard leads to its compaction causing the surface subsidence (Santoyo et al., 2005). The subsidence is damaging key urban structures of the city such as domestic and historical buildings, water supply pipes, drainage pipes, gas, electricity and telephone installations (Santoyo et al., 2005). It also creates depressions (up to 30 m registered in Azcapotzalco over the last century, Carrera-Hernández and Gaskin, 2007) in some areas of the basin, which are now prone to inundations. In order to assess the risks at stake in the Mexico Basin, the subsidence phenomenon needs to be accurately mapped and analyzed through space and time.

Radar interferometry (InSAR, Interferometric Synthetic Aperture Radar) has been successfully applied to map subsidence caused by water pumping, using both a small baseline interferograms approach (Berardino et al., 2002; Schmidt and Bürgmann, 2003; Usai, 2003) or the Permanent Scatterer method, (Ferretti et al., 2000). The first method uses coherent interferograms issued from short perpendicular

* Corresponding author. Laboratoire de Geologie, École Normale Supérieure, CNRS UMR 8538, Paris, France.
E-mail address: penelope@centrogeo.org.mx (P. López-Quiroz).
[1] Present address: Centro de Investigacion en Geografia y Geomatica "Ing. Jorge L. Tamayo", A.C., Contoy 137 Lomas de Padierna, CP 14240, Mexico DF. MEXICO.

0926-9851/$ – see front matter
doi:10.1016/j.jappgeo.2009.02.006

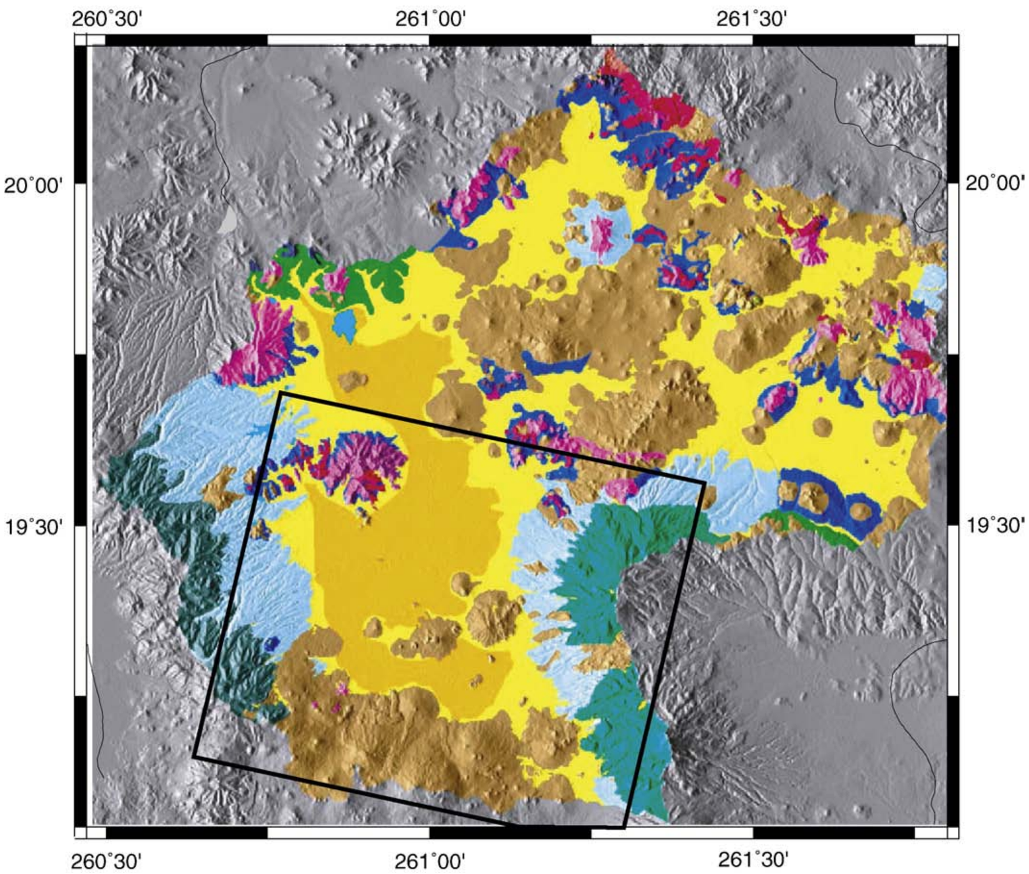

Fig. 1. Main hydrogeological units and SRTM elevation relief adapted from Carrera-Hernández and Gaskin (2007). 1) Alluvial sediments or aquifer layer (Yellow). 2) Lacustrine sediments or aquitard layer (Orange) partially covering the aquifer. 3) Basalt and vulcanites (Brown and other colors). Black square shows the studied area. (For interpretation of the references to color in this figure legend, the reader is referred to the web version of this article.)

baseline image pairs. Multilooked and/or filtered interferograms are unwrapped individually before being inverted to obtain deformation time series with some mitigation of atmospheric perturbations. The second method uses all available images to construct interferograms with respect to a common master. The amplitude (Ferretti et al., 2001) or both, amplitude and phase (Hooper et al., 2004), are used to select pixels not affected by spatial and temporal decorrelation, thus carrying reliable phase information. The corrected height is estimated for each "persistent scatterer" (PS). Temporal (1D) or sometimes spatio-temporal (3D) unwrapping methods are then used to unwrap the phase on the PS network (Hooper and Zebker, 2007), to recover radar propagation delays and finally to separate the deformation signal from atmospheric perturbations. In the present work we choose to use a method using small baseline interferograms inspired from the work presented by (Cavalié et al., 2007), where the correction of residual orbital and atmospheric fringes on interferograms is performed before inversion. Their method is also employed to test the misclosure in the redundant interferometric system.

Previous works measuring the Mexico City subsidence by interferometry (Strozzi et al., 2003; Cabral-Cano et al., 2006) focused on the generation of a reduced number of highly coherent interferograms with short time span (1 month) and limited in space (downtown and west part of the city). No time series analysis able to precisely map the Mexico City subsidence in time and space has to our knowledge been published until now. We believe that this lack of temporal analysis is due to the coherence loss and the high number of fringes present on interferograms with large temporal baselines making the unwrapping step extremely difficult. In this work, we present an iterative method to overcome the faced unwrapping problems. This method could be generalized to other areas showing stable ground displacement patterns. We also propose a new algorithm to invert interferograms into time series more suited to the Mexico City SAR data base than the SVD decomposition proposed in (Berardino et al., 2002) or (Schmidt and Bürgmann, 2003). Finally, we derive the temporal behavior of the subsidence from end of 2002 to beginning of 2007 over the whole metropolitan area of the city at a resolution of 30 × 30 m. A global view of the main processing steps achieved is available on Fig. 2.

2. Interferogram processing

2.1. Interferogram formation

In this study, a four year ENVISAT archive of 39 images centered on Mexico City was provided by the European Space Agency (ESA). Those images were acquired between November 2002 and March 2007. To construct interferograms, and because of the coherence loss and the high subsidence rates, we limit image pairs to those having temporal baselines (B_t) lower than 9 months and perpendicular baselines ($B_\perp$) lower than 500 m. We build a total number of 71 interferograms from 38 images that provide links between all 38 acquisition dates (see Fig. 3).

We use the JPL/CalTech Repeat Orbit Interferometry Package (ROI_PAC) (Rosen et al., 2004) to construct the differential interferograms and unwrap them. Orbital fringes are removed using orbits provided by the Department of Earth Observation and Space Systems (DEOS) of the Delft University of Technology (Scharroo et al., 1998). The topographic contribution is removed using the 3-arc second sampled Shuttle Radar Topography Mission (SRTM) digital elevation model (DEM) (Farr and Kobrick, 2000). Multilooking of a factor 5 was applied to the interferograms along the azimuth leading to a ground

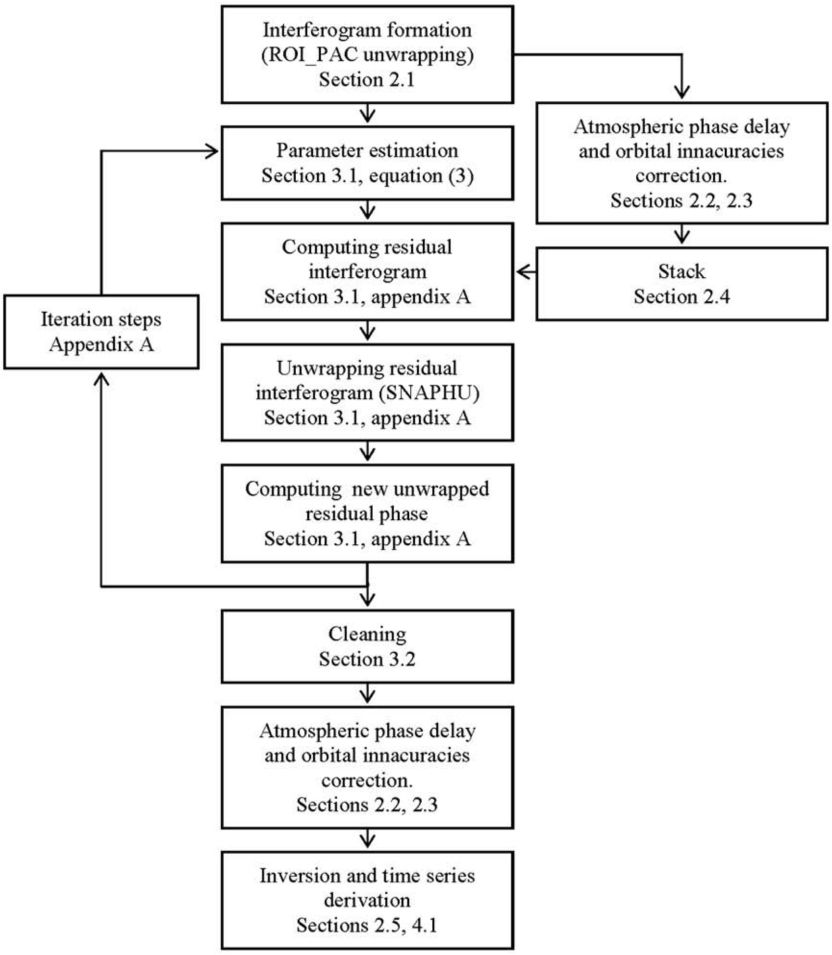

Fig. 2. Main processing steps and corresponding document sections.

pixel resolution of ~20 m × 20 m. A nonlinear adaptive spatial filtering (Goldstein and Werner, 1998) was applied to each interferogram to increase the signal to noise ratio. Note that geocoding is applied at the very end of the data analysis, after inversion into time series. All analysis is thus performed in radar geometry, put back in the geometry of a "master" image by amplitude image correlation.

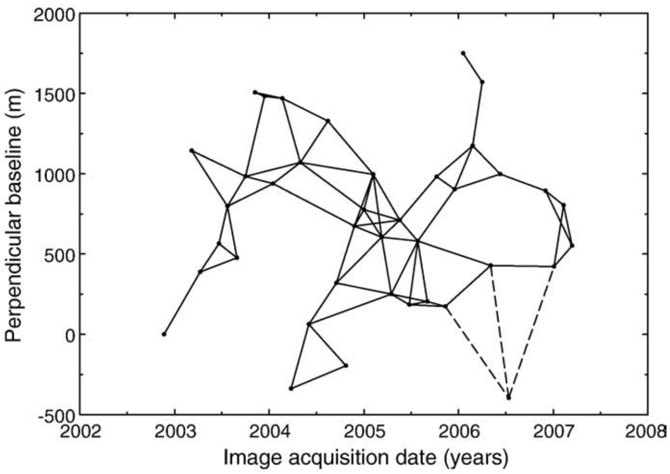

Fig. 3. Images and interferograms database. The points represent the 39 image acquisition dates. The solid lines represent the 71 interferograms performed in the present study. The dashed lines show a set of interferograms with $B_{\perp} > 500$ m which cannot be used due to geometrical decorrelation. Those interferograms would link the 71 interferograms set with the July 2006 image of the database. Finally, only 38 images can be used.

The flattened and topographically corrected interferogram phase, ϕ_{ifg}, can be split into the sum : $\phi_{\text{ifg}} = \phi_{\text{def}} + \phi_{\text{atm}} + \phi_{\text{orb}} + \phi_{\text{DEM}} + n$, where ϕ_{def} is the phase change due to the ground displacement in the satellite line-of-sight (LOS) direction, ϕ_{atm} is the phase due to differential atmospheric delay between the two passes, ϕ_{orb} is the residual phase due to orbit inaccuracies, ϕ_{DEM} represents residual DEM errors and n is the noise phase. Examples of the best Mexico City interferograms are shown on Fig. 4. They are unwrapped without errors using the branch-cut algorithm (Goldstein et al., 1988) provided by ROI_PAC, then corrected from the atmospheric phase delay and orbital inaccuracies as described in the following two sections. Each interferogram is identified trough a pair of image acquisition dates (yyyymmdd). These interferograms cover 35 to 70 days time intervals during winter 2003–2004 and winter 2004–2005. The deformation is concentrated in the flat lacustrine area of the basin at an elevation lower than 2250 m, on the location of the former lakes (see Fig. 1).

2.2. Correction of stratified atmospheric phase delay

It is possible to classify the atmospheric contributions into turbulent mixing and vertical stratification contributions (Hanssen, 2001). The former is the result of turbulent processes in the atmosphere, the latter results from different vertical refractivity profiles during the two SAR acquisitions. Because of their nonlinear nature, turbulent processes affect the interferometric signal on a wide range of scales and are

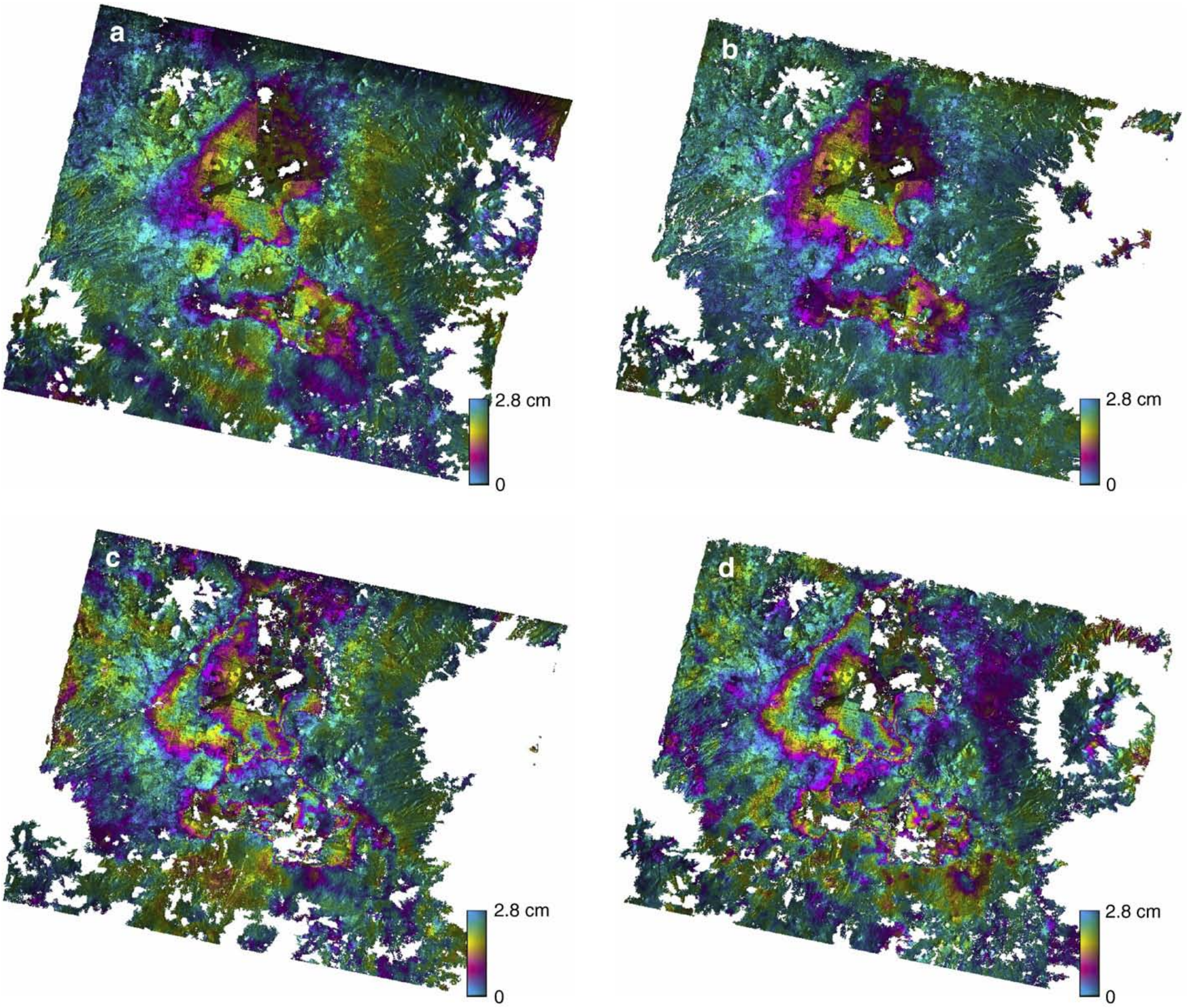

Fig. 4. Examples of differential interferograms for time spans a) 20031107–20031212 and b) 20041231–20050204, integrating deformation for 35 days, c) 20041231–20050311 and d) 20031212–20040220 showing the deformation for 70 days. Interferograms are processed by ROI_PAC, then corrected from the stratified atmospheric phase delay and the residual orbital errors. Note that the shape of the deformation on each interferogram is very similar. Areas with coherence loss are displayed in white. For geographical location, see Fig. 1. (For interpretation of the references to color in this figure legend, the reader is referred to the web version of this article.)

difficult to model. Currently, no methods are able to quantify them accurately and routinely (Wadge et al., 2002; Puysségur et al., 2007), so most of the studies consider it as a random signal or noise affecting interferograms. In this study, we only correct interferograms from the vertical stratification contribution and consider turbulent contributions as a random phase both in space and time. The vertical stratification contribution is correlated with elevation (Delacourt et al., 1998; Beauducel et al., 2000; Chaabane et al., 2007), as the delay in the radar microwave propagation from the satellite to the ground depends on the integrated atmospheric water vapor content, dependent upon the scene elevation.

Because the subsidence is concentrated over the flat area of the basin, the deformation signal is not affected by stratified atmospheric artifacts. However, it is important to remove the stratified contribution outside the lacustrine basin, since it is significant in some interferograms and it can affect the phase estimation in areas assumed without deformation that are used to refer displacement. We estimate the vertical stratification contribution on each interferogram by performing a linear regression between the interferometric phase and the elevation (as in Cavalié et al., 2007, see Fig. 5), taking into account all unwrapped pixels but those located in the nearly flat area.

2.3. Orbital inaccuracies correction

Orbital parameters used to flatten interferograms are not accurate enough to completely remove orbital fringes from interferograms during the conventional processing performed by ROI_PAC. The residual orbital ramp represents one or two fringes at most. In order to remove the residual orbital errors, ϕ_{orb}, we estimate the best fitting 'twisted plane' (Cavalié et al., 2007) to the phase delay away from the deformation zone. The 'twisted plane' is represented by $\phi_{\mathrm{orb}} = (ax + b)y + cx + d$, where x and y are the range and azimuth coordinates. A median filter weighted by coherence is first applied to the interferograms to decrease the influence of outliers. As the residual ramp and the atmospheric phase contribution are better estimated simultaneously than successively, we adjust $\phi_0 = (ax + b)y + cx + d + \beta z$ for $z > 2250$ m to the interferometric phase, where z is the elevation and a, b, c, d and β are obtained using a least square minimization. Note that very large scale features in atmospheric

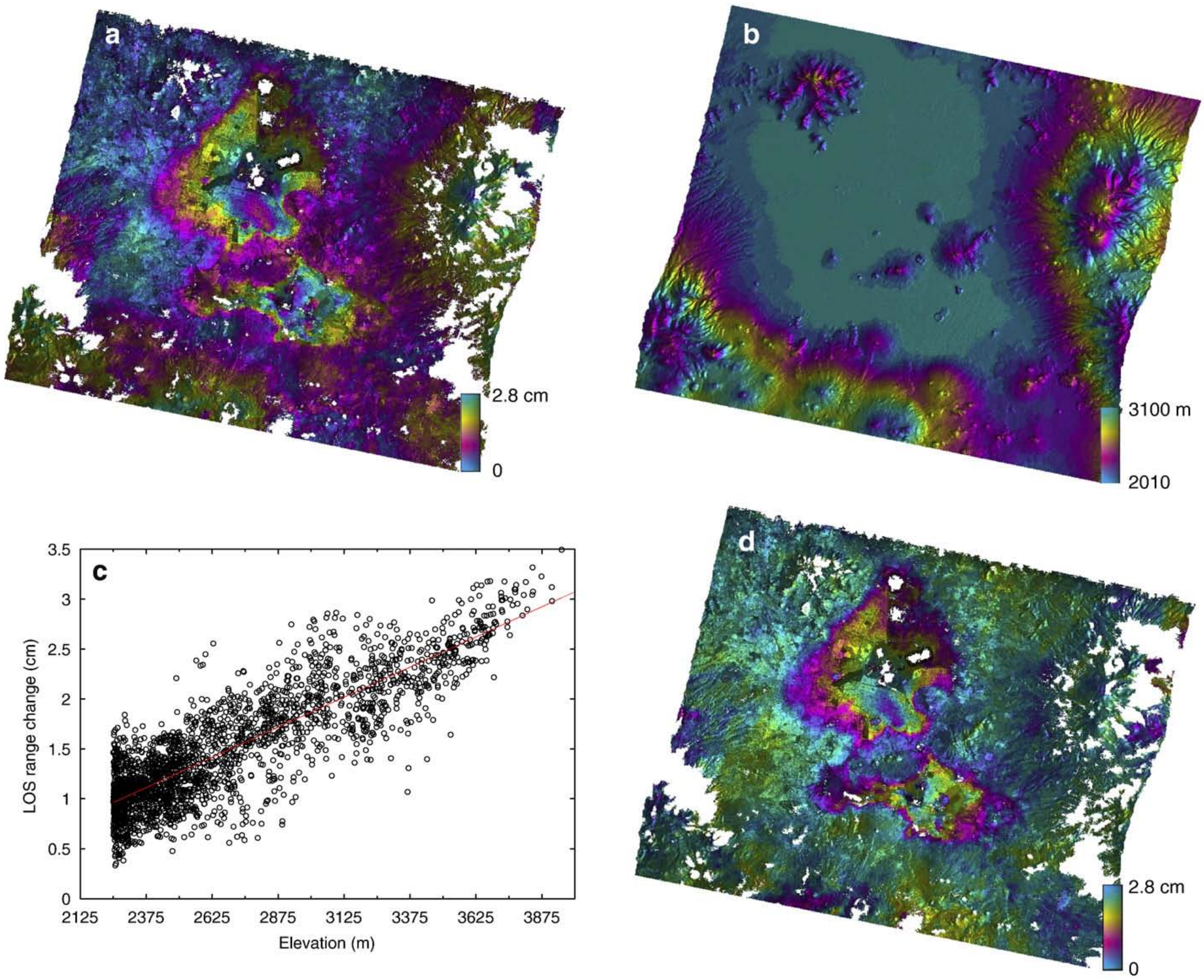

Fig. 5. a) Original interferogram 20041126–20041231. The interferometric phase increases gradually as elevation increases on volcanoes flanks outside the Mexico lacustrine basin area. b) DEM of the corresponding area. c) Interferometric elongation path measured in the Satellite Line Of Sight (LOS) plotted versus elevation. The flat area (elevation lower than 2250 m), where the subsidence phenomenon principally occurs, is excluded to perform the linear regression shown by the red line. d) Interferogram corrected from the stratified atmospheric contribution and the residual orbital ramp. The phase outside the deformation area is near to zero on average. For geographical location, see Fig. 1. (For interpretation of the references to color in this figure legend, the reader is referred to the web version of this article.)

propagation delays, if non negligible, could also be partially included in the adjusted phase ramp, together with the residual orbital ramp. Removing these contributions allows us to work with flattened interferograms showing a deformation referred to the areas with elevation larger than 2250 m where the average phase is set to zero.

2.4. Stack

We select the best five interferograms corresponding to the winter periods: 20031107–20031212, 20031212–20040220, 20041126–20041231, 20041231–20050204, 20041231–20050311 (see Figs. 4 and 5), and stack them to represent the deformation occurring in 35 days (see Fig. 6). All of them are flattened and unwrapped without noticeable errors using ROI_PAC, their small temporal baselines, B_t, of 35 or 70 days insuring a good phase continuity. They are then corrected from atmospheric delays and orbital errors as explained previously.

Even if they represent the deformation occurring during two different winters, 2003–2004 and 2004–2005, they show similar deformation patterns (see Figs. 4 and 5). The good correlation of the ϕ_i phase of the ith differential interferogram with the ϕ_1 phase of the 20041231–20050204 "reference" interferogram allows to define a regression coefficient α_i between ϕ_i and ϕ_1. All differential interferograms (especially those with B_t of 70 days) are then scaled by this factor α_i yielding the same deformation amplitude as in the 20041231–20050204 "reference" interferogram. After this normalization, we can stack them and compute the average phase for each pixel l, $\phi^l_{\text{stack}} = \frac{1}{N_l}\left[\phi_1 + \sum_{i=2}^{N_l} \alpha_i \phi_i\right]$ where N_l is the number of interferograms with a valid phase for the pixel l. The delay obtained for each interferogram and the stack are displayed in Fig. 7 along the profile shown on Fig. 6. Shaded segments on Fig. 7 highlight the higher elevation areas where no deformation occurs. Very high deformation gradients are present in the flanks of these volcanoes, reaching up to 2.5 cm (~1 fringe) for 35 days across 210 m (~10 pixels). Note that due to the mitigation of stratified atmospheric contributions and residual orbital ramp, the delay is flat and close to zero on all interferograms outside the deformation area. To avoid noise contamination in the following use of the stack, it is strongly smoothed by applying the nonlinear adaptive ROI_PAC filter (Figs. 6 and 7, black solid line).

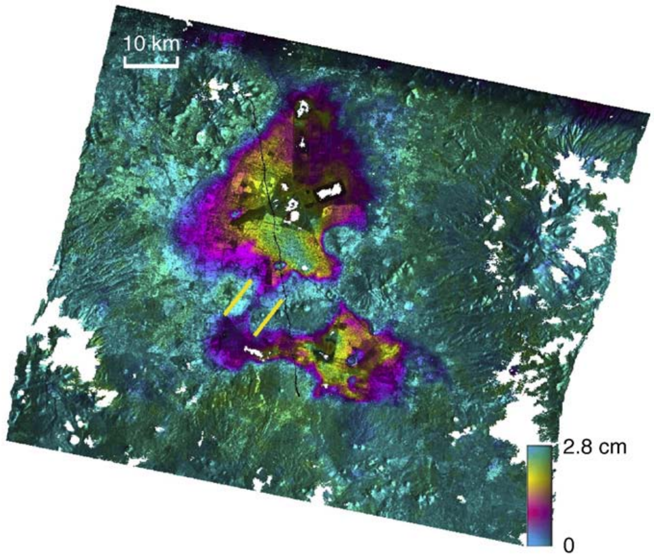

Fig. 6. Stack of the 5 best interferograms. Unwrapped and corrected interferograms shown on Figs. 3 and 4 are used to produce a stack representing the averaged deformation phase for 35 days. The black line shows the localization of the profiles shown in Fig. 7. The area between the two parallel yellow lines is a very narrow corridor presenting large deformation gradients across which several unwrapping errors occurred on numerous processed interferograms. This narrow corridor links the two main subsidence areas.

2.5. Inversion

Once all interferograms were unwrapped using ROI_PAC, we obtain the phase delay time series by least square inversion, treating each pixel independently from its neighbors (Cavalié et al., 2007). For a given pixel, l, the number of valid interferograms, N_l, and the number of images, M_l, included in those interferograms may be smaller than the total interferogram number N and the total image number M. They depend on the pixel location as some interferometric links shown in Fig. 3 may not be valid for pixel, l. We solve for each pixel, l, the linear equation

$$\boldsymbol{d}_l = \mathbf{G}_l \boldsymbol{m}_l \tag{1}$$

where $\boldsymbol{d}_l$ is the vector including the data, i.e., the phase of N_l interferograms for pixel l; $\boldsymbol{m}_l$ is a vector containing the unknowns, i.e., the $M_l - 1$ phase delay increments for pixel l between two successive images; $\mathbf{G}_l$ is a $N_l \times (M_l - 1)$ matrix of zeros and ones, constructed based on the fact that the phase of an interferogram, ϕ_{ij}^l, is the sum of the successive phase delays between images i and j: $\phi_{ij}^l = \Sigma_{k=i}^{j-1} m_k^l$. The inversion is applied to all pixels provided that the coherence at the pixel location is good enough for at least 40 interferograms of the data base. For a relatively large number of inverted pixels, the system is underdetermined, i.e. $\mathbf{G}_l^{\mathbf{T}} \mathbf{G}_l$ is singular. The singular value decomposition (SVD) method is then used instead of the least squares method to solve $\boldsymbol{d}_l = \mathbf{G}_l \mathbf{m}_l$.

2.6. Identification of unwrapping errors

When interferograms present some redundancy, unwrapping errors can be detected through inconsistencies in the interferometric data set. To evaluate the temporal closure of the interferometric system on each pixel, we calculate for all interferograms, N, the root mean square, RMS, between the observed interferogram phase, ϕ_{ij}, and the one reconstructed from inverted successive phase delays (Cavalié et al., 2007):

$$\phi_{\mathrm{RMS}_{\mathrm{pixel}}^l} = \frac{1}{N_l}\left[\sum_{N_l}\left(\phi_{ij}^l - \sum_{k=i}^{j-1} m_k^l\right)^2\right]^{1/2} \tag{2}$$

To estimate how a given interferogram fits into the interferometric system, we also compute the RMS for all valid pixels P of the interferogram: $\phi_{\mathrm{RMS}_{\mathrm{ifg}}}^{ij} = \frac{1}{P}\left[\sum_l \left(\phi_{ij}^l - \sum_{k=i}^{j-1} m_k^l\right)^2\right]^{1/2}$. Finally, we also study the deviation map $|\phi_{ij}^l - \Sigma_{k=i}^{j-1} m_k^l|$ for each interferogram to

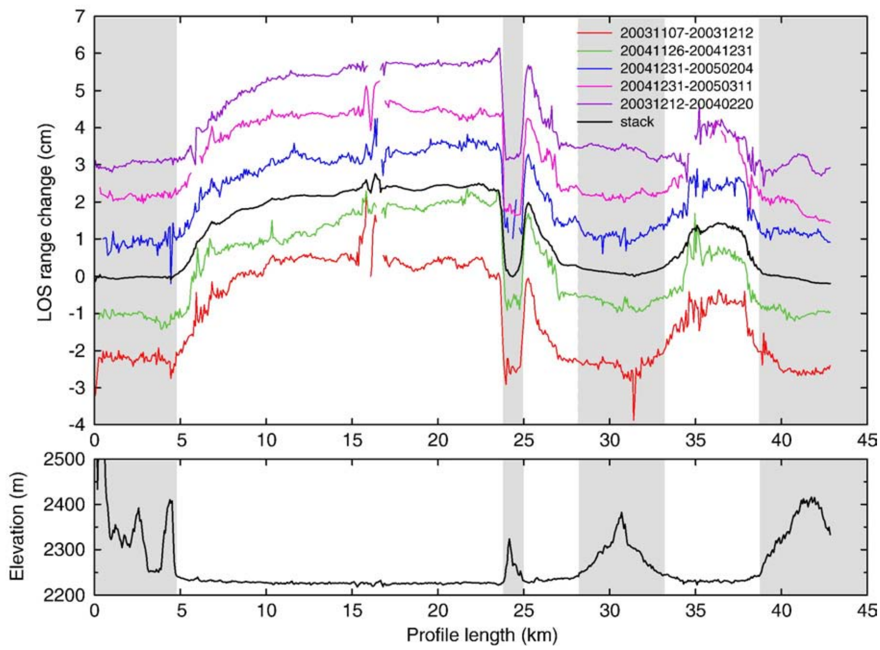

Fig. 7. Profile across the filtered stack (black solid line) and the individual interferograms (color lines). All profiles are scaled to correspond to displacement occurring for 35 days. The profiles have been translated by 1 cm for clarity. Shaded areas correspond to elevation larger than 2250 m where no deformation occurs.

identify where discrepancies occur and thus to isolate the locations of unwrapping errors.

Fig. 8a shows the global $\phi_{RMS_{pixel}}$ map resulting from the inversion of the interferograms unwrapped using the ROI_PAC branch-cut algorithm. The RMS increases from black to white and indicates that large and numerous unwrapping errors are present in the produced interferograms. Fig. 8b shows the RMS for each interferogram, $\phi_{RMS_{ifg}}$, that peaks for interferograms 2 and 3 as well as for interferograms 25 and 32 denoting inconsistencies due to unwrapping errors occurring in some of them. Fig. 8c displays the deviation map for interferogram 3, which includes some of the large RMS value patterns shown on Fig. 8a. An inspection of the interferogram (Fig. 8d) indicates the location of large and unusual unwrapping errors responsible for high RMS patches. A more typical unwrapping problem, occurring on interferogram 25, is shown in Fig. 8e and f. The deviation map displays both a tilt and a sudden RMS change across a curved line (in yellow) due to an unwrapping error (Fig. 8f). As a result, the East–West interferogram flattening is not consistent with the whole interferogram data set and

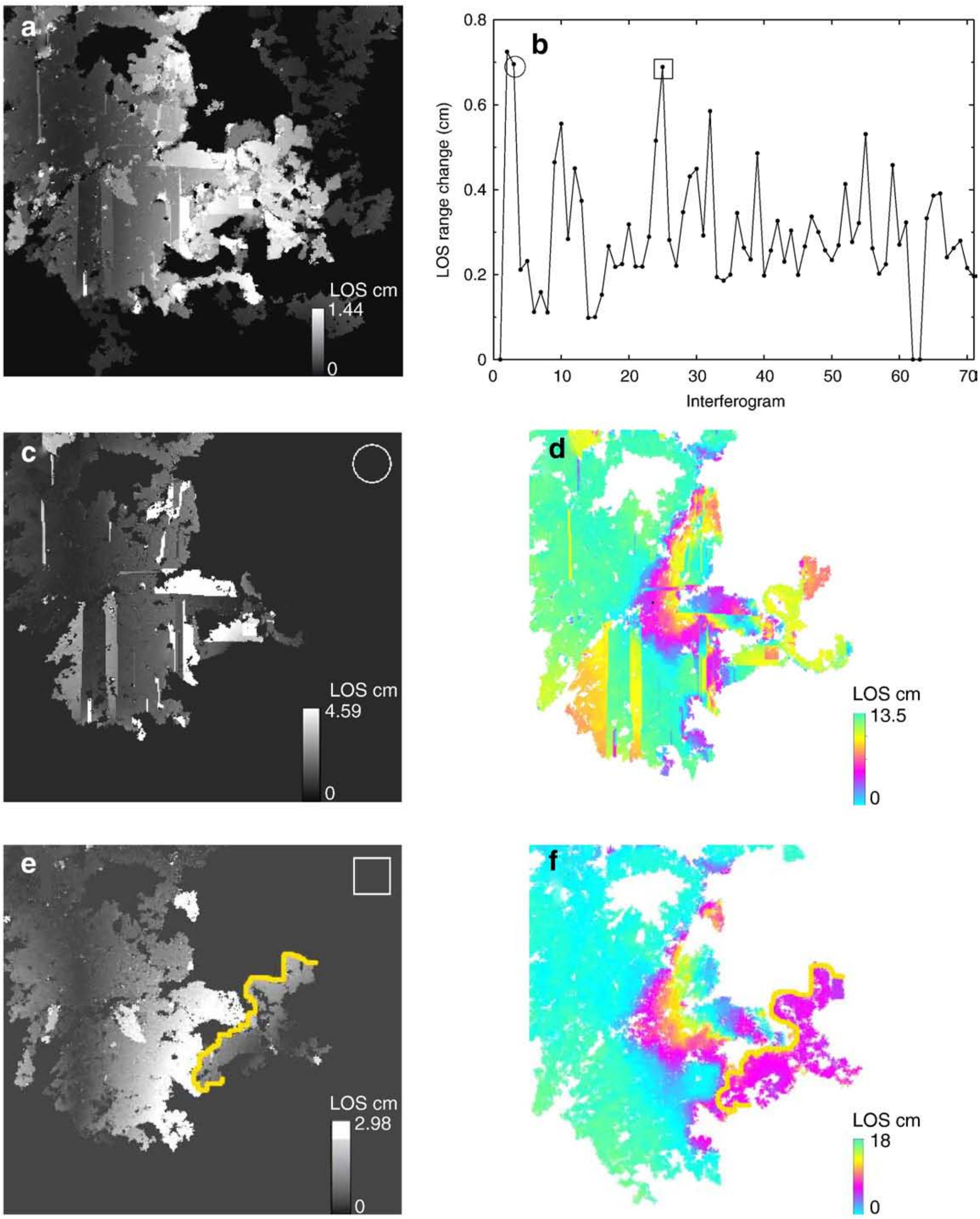

Fig. 8. a) Map of $\phi_{RMS_{pixel}}$ describing the discrepancies in the network of interferograms unwrapped using the ROI_PAC branch-cut algorithm. The RMS increases from black to white areas. b) RMS of the inversion for each interferogram, $\phi_{RMS_{ifg}}$. Two peaks denoted ○ and □ are analyzed in the next panels. c) Deviation map of interferogram 3 (○: 20030307–20031003) displaying some of the patterns seen in (a). d) Interferogram 3 unwrapped with ROI_PAC showing large unwrapping errors. e) Deviation map for interferogram 25 (□: 20040430–20050204) displaying a tilt and a phase jump across the yellow line. f) Corresponding interferogram with an unwrapping error delineated by the yellow line. (For interpretation of the references to color in this figure legend, the reader is referred to the web version of this article.)

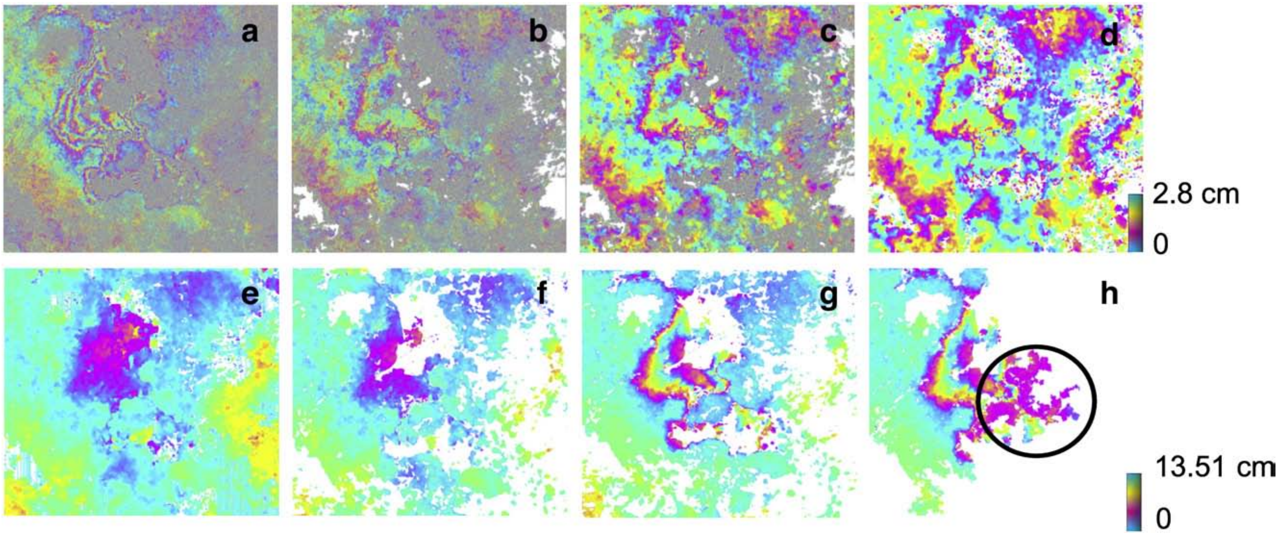

Fig. 9. a) Wrapped unfiltered interferogram phase, $e^{i\phi_{\rm ifg}}$. b) Wrapped residual interferogram, $e^{i\phi^{1}_{\rm res}}$, after removal of the stack scaled by α_1. In this first iteration, α_1 is slightly underestimated: part of the deformation is still present in the residual interferogram. c) ROI_PAC adaptive filter applied to the wrapped residual interferogram, $e^{i\phi^{\rm adf}_{\rm res}}$. d) Low-pass filtered residual interferogram, $e^{i\phi^{\rm lp}_{\rm res}}$. e) Residual phase, $\phi^{\rm lp_{unw}}_{\rm res}$, unwrapped using SNAPHU. f) Unwrapped residual phase, with a mask corresponding to areas without coherence in (c), on which the high frequencies of (d)–(e) are added back, $\phi^{\rm adf_{unw}}_{\rm res}$. g) Filtered unwrapped interferogram phase, $\phi^{2}_{\rm unw}$, on which the scaled stack version is added back. h) Interferogram unwrapped with ROI_PAC branch-cut method shown for comparison with (g). The unwrapping error (within the black circle) has disappeared in (g). See Appendix A for explanation.

produces the tilt in the deviation map seen in Fig. 8e. These unwrapping errors occur along the high deformation gradient channel shown surrounded by yellow lines in Fig. 6. This kind of analysis was repeated for all produced interferograms. It is clear that unwrapping errors seriously compromise the quality of the displacement maps that could be obtained. In the next section, we present a method to guide interferogram unwrapping.

3. Solving unwrapping problems

The main problem of the Mexico City interferogram processing is the unwrapping step, not because of the lack of robustness of the ROI_PAC branch-cut algorithm (which is from our experience quite reliable) but because of the coherence loss and mostly the high number of fringes and large fringe gradients present in interferograms. Deformation gradients are so high that they locally reach one fringe every two pixels (the aliasing rate) for 1 yr interferogram. For interferograms with temporal baseline larger than 70 days, coherence decreases while the number of fringes increases. Unwrapping then becomes extremely difficult and a method to guide it is necessary (Yun et al., 2007; Pinel et al., 2007).

3.1. Principles of the iterative unwrapping procedure

Our method relies on the observation that the spatial pattern of the deformation extracted from each interferogram is, at first order, stationary for a given time interval during all the studied period. Let us thus decompose the deformation, $D(x, y, t)$, into a component with a stationary shape, $F(x, y)$, modulated by an a priori unknown time function, $T(t)$, and a second order deformation term, $F'(x, y, t)$:

$$D(x,y,t) = F(x,y)T(t) + F'(x,y,t). \qquad (3)$$

The interferogram stack described above can be used as a proxy for the deformation shape, $F(x, y)$. As the variation of $T(t)$ between two acquisition dates is a priori unknown, we estimate it from the data by computing the regression coefficient, α, between the interferometric phase, $\phi_{\rm ifg}$, and the stack phase, $\phi_{\rm stack}$. In theory, α could be positive or negative depending on whether $T(t)$ is, or not, monotonous in time.

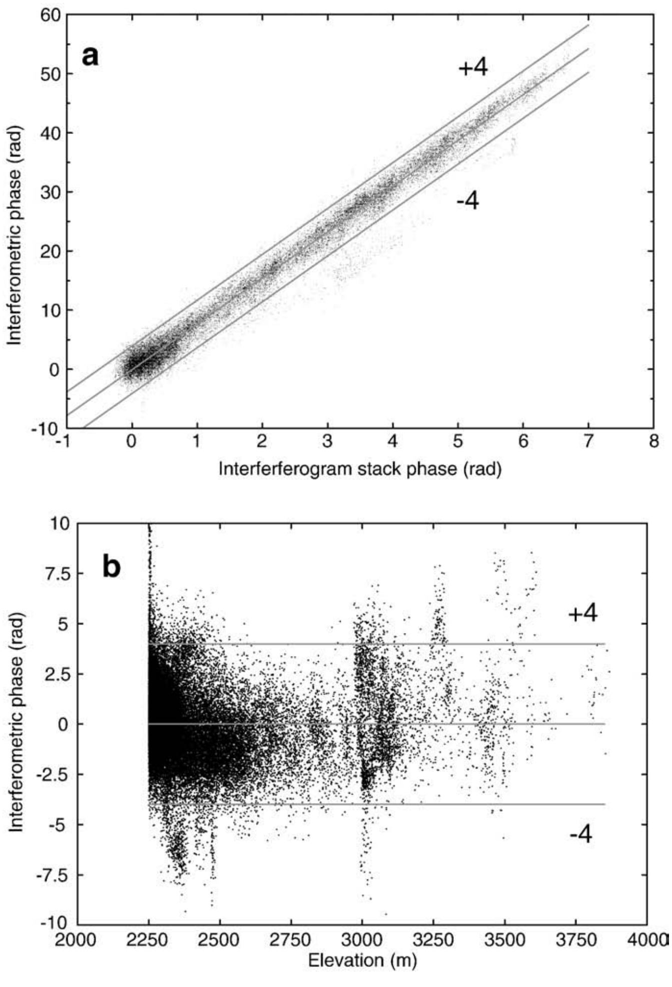

Fig. 10. a) Phase delay versus stack phase (the slope of the fitted line is α_3). b) Phase delay versus elevation (the slope of the fitted line is β_3). The cleaning step consists in masking all phase data outside the ± 4 rad interval from the fitted line.

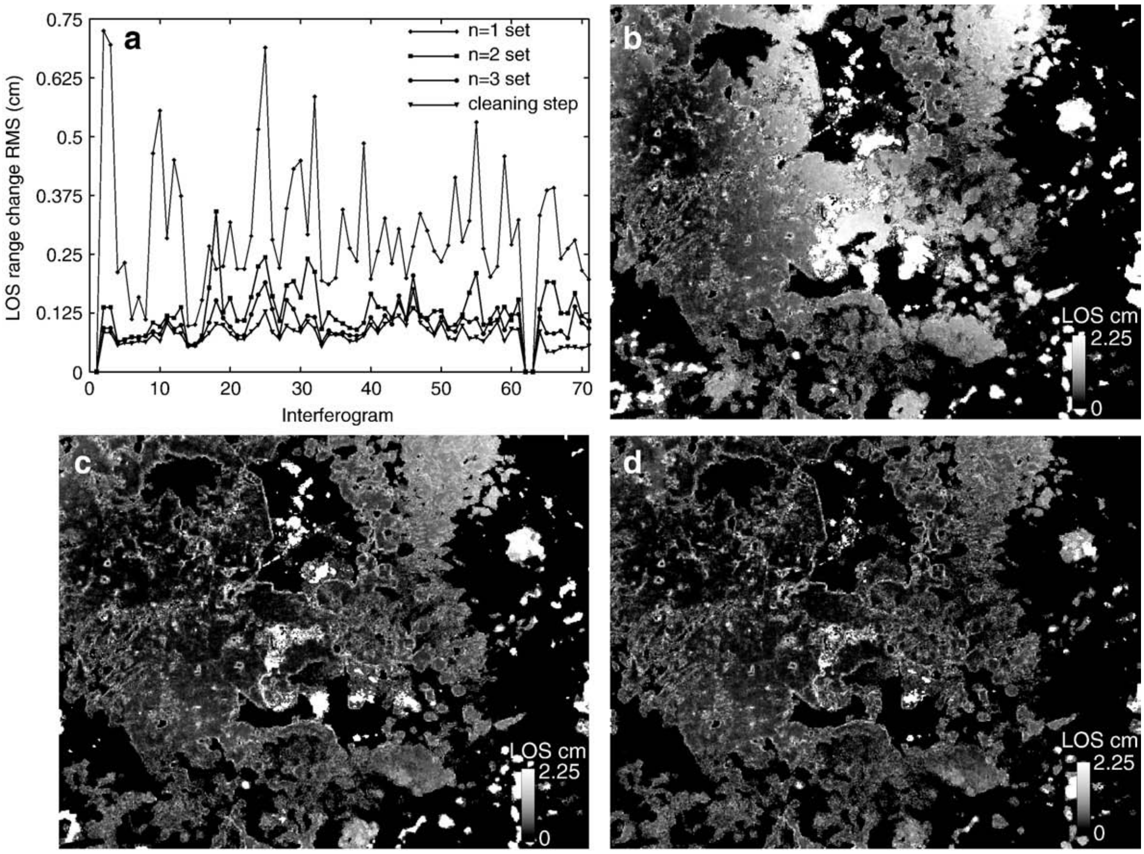

Fig. 11. a) Evolution of the misclosure of the interferometric data set, $\phi_{\mathrm{RMS}_{\mathrm{ifg}}}$, from sets 1 to 3, and after "cleaning". The RMS values show in general a large decrease from ROI_PAC iteration ($n=1$) to the next unwrapping iterations. This expresses a large improvement of the interferograms unwrapping quality. Further improvement is obtained for sets 2 and 3 and after the cleaning step. b) Map of system misclosure $\phi_{\mathrm{RMS}_{\mathrm{pixel}}}$ for the interferograms set $n=2$. c) $\phi_{\mathrm{RMS}_{\mathrm{pixel}}}$ for set $n=3$. d) $\phi_{\mathrm{RMS}_{\mathrm{pixel}}}$ after "cleaning".

However, as will be seen below, we find that α is always relatively close to the value expected for $T(t)$ linear in time.

We therefore describe the interferogram phase as:

$$\phi_{\mathrm{ifg}} = \underbrace{\alpha\phi_{\mathrm{stack}}}_{\mathrm{def}} + \underbrace{(ax+b)y+cx+d}_{\mathrm{orbital}} + \underbrace{\beta z}_{\mathrm{atm_{vert}}} + \underbrace{\phi_n}_{\mathrm{def,atm_{turb},DEM_{error},noise}} \quad (4)$$

where $\alpha\phi_{\mathrm{stack}}$ is the scaled stack phase representing the main part of the deformation, $(ax+b)y+cx+d$ is the residual orbital contribution, βz is the stratified atmospheric contribution and ϕ_n is the phase containing the deformation that does not follow the stack shape, turbulent atmospheric noise, DEM errors and phase noise (thermal noise, coregistration errors, etc.).

To guide unwrapping, we construct the residual wrapped interferogram $e^{i\phi_{\mathrm{res}}}$ from the wrapped unfiltered raw interferogram $e^{i\phi_{\mathrm{raw}}}$:

$$e^{i\phi_{\mathrm{res}}} = e^{i(\phi_{\mathrm{raw}} - \alpha\phi_{\mathrm{stack}} - \beta z)}. \quad (5)$$

We observe that the wrapped residual has less fringes and relatively smoother phase gradients than the original interferogram and is easier to unwrap. This confirms that $\alpha\phi_{\mathrm{stack}}$ indeed corresponds to the main deformation component and that removing the wrapped scaled stack, $e^{i\alpha\phi_{\mathrm{stack}}}$, does not add phase noise to the original interferogram.

However, the parameters α and β must be first evaluated on a previously obtained unwrapped interferogram, ϕ_{unw}. We thus perform the following steps iteratively:

(1) Estimate parameters α_n and β_n using Eq. (4) and the unwrapped interferogram phase from the previous step ϕ^n_{unw}
(2) Compute the residual interferogram $e^{i\phi^n_{\mathrm{res}}} = e^{i(\phi_{\mathrm{raw}} - \alpha_n\phi_{\mathrm{stack}} - \beta_n z)}$
(3) Unwrap the residual interferogram $e^{i\phi^n_{\mathrm{res}}}$ as described in Appendix A.2. At the end of this step, the unwrapped residual phase, $\phi^n_{\mathrm{res_{unw}}}$, is filtered with the ROI_PAC nonlinear adaptive filter. Fig. 9 displays the different steps of the residual phase unwrapping.
(4) Compute the new unwrapped filtered phase with $\phi^{n+1}_{\mathrm{unw}} = \phi^n_{\mathrm{res_{unw}}} + \alpha_n\phi_{\mathrm{stack}} + \beta_n z$.

Note that the scaling factor, α_n, is a free parameter that does not preclude for the subsidence temporal evolution. As it is the same for the whole image, it implies that the unwrapped residual, $\phi^n_{\mathrm{res_{unw}}}$, contains the spatial part of the deformation that is not proportional to the stack. Therefore, the new unwrapped phase $\phi^{n+1}_{\mathrm{unw}}$ is not constrained to follow any particular temporal or spatial shape by the unwrapping procedure provided that deformation gradients in the residual interferogram are moderate enough for unwrapping to proceed without errors. Steps (1) to (4), embedded into two iterations, are described in Appendix A.1 with more details.

3.2. Cleaning step

After applying the iterative unwrapping steps, most unwrapping errors are removed from interferograms. Unfortunately, locally, some errors still remain. These errors can be detected in deviation maps but also as secondary trends in plots of the phase delay versus stack phase or versus elevation (see examples on Fig. 10). We decide to mask in every interferogram all pixels for which the phase $\phi_n = \phi^3_{\mathrm{unw}} - \alpha_3\phi_{\mathrm{stack}} - (a_3x + b_3)y - c_3x - d_3 - \beta_3 z$ has an amplitude larger than 4 radians. This last step only removes phase values on some pixels that do not appear as reliable.

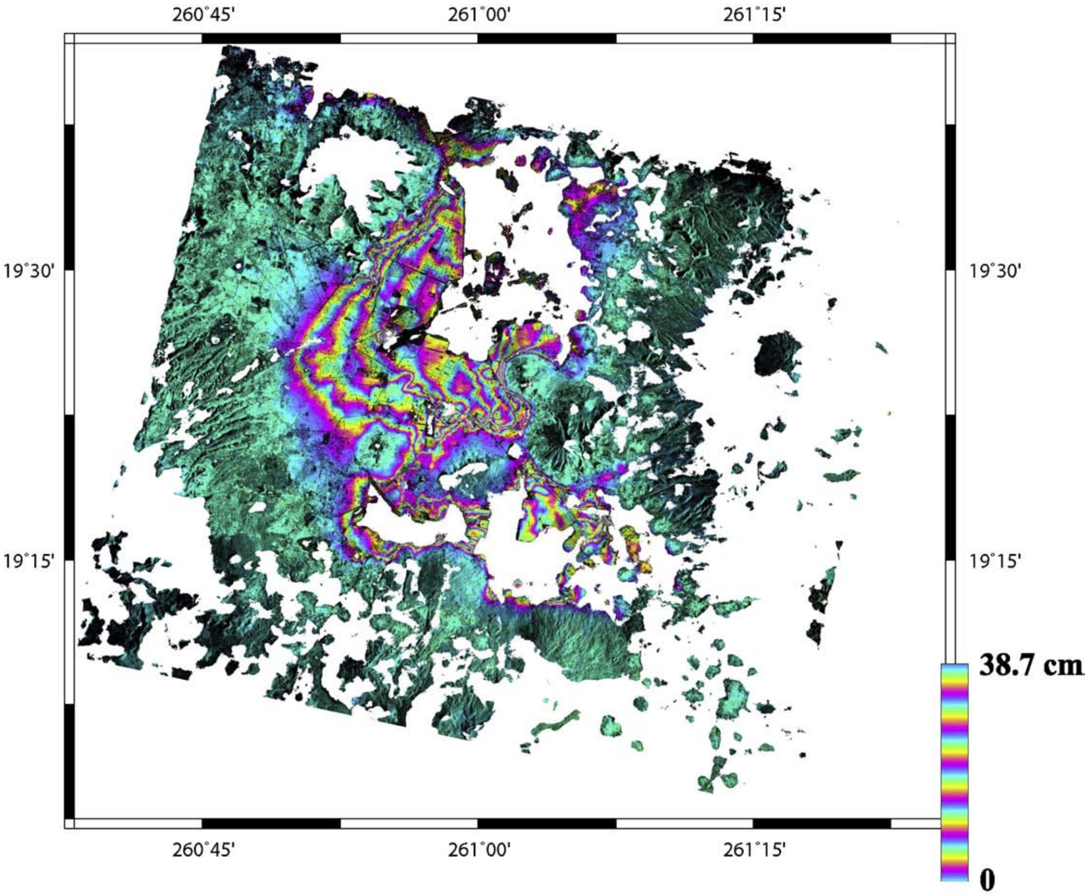

Fig. 12. Average vertical subsidence rate of the Mexico City metropolitan area for the period 2003–2007, superimposed on a radar backscatter amplitude map.

3.3. Unwrapping results analysis

Fig. 11a shows the evolution of inconsistencies in the interferometric data set, $\phi_{\mathrm{RMS_{ifg}}}$, from sets 1 to 3 and after the cleaning step. The RMS values show in general a large decrease from the first set unwrapped with ROI_PAC to the second set. This means that numerous unwrapping errors are removed when unwrapping is "guided" by the stack. This improvement continues from the second to the third step, and after the cleaning step.

Fig. 11b shows the RMS misclosure, $\phi_{\mathrm{RMS_{pixel}}}$, corresponding to the second interferogram set. Light areas mark the locations, as in recently urbanized or vegetated areas, where the noise due to temporal decorrelation impedes correct unwrapping. The extent of these areas is strongly decreased in the third interferogram set (Fig. 11c). Applying the cleaning step solves almost all the remaining discrepancies in the unwrapped data set (Fig. 11d).

4. Time series analysis

4.1. Method to derive subsidence time series

Time series of the phase delay have first been obtained from the inversion described in Section 2.5 and Eq. (1) for 6×10^6 20×20 m^2 pixels, i.e., covering about 50% of the studied surface. They show a remarkably linear subsidence through time. However, for 42% of the inverted pixels, $\mathbf{G}_l^{\mathbf{T}}\mathbf{G}_l$ has a rank deficiency, i.e. at least a critical link in the interferogram network is missing. In these cases, the acquisition data set is split into two or more independent image groups and SVD is used instead of least squares to retrieve the delay time series (Berardino et al., 2002). In the present study, due to the particular graph configuration of Fig. 3, groups of independent images often present no temporal (B_t) or geometrical ($B_\perp$) overlaps. The incremental phase delay between successive image groups is then set to zero by SVD. It biases the subsidence temporal behavior and thus the subsidence rate.

To overcome this problem, instead of using SVD, we add constraints to the inversion. Let us first define the cumulated phase delay at time t_k for pixel l, ϕ_k^l, by:

$$\phi_k^l = \sum_{i=1}^{k-1} m_i^l \qquad \text{for } M_l \ge k \ge 2$$

$$\phi_1^l = 0$$

where m_i^l are the phase delay increments, for pixel l, between two successive acquisitions. Inspection of previous delay time series, for pixels for which $\mathbf{G}_l^{\mathbf{T}}\mathbf{G}_l$ is invertible, shows that modeling ϕ_k^l by a quadratic behavior in time is reasonable. The residual with respect to a quadratic behavior in time is, for the vast majority of these pixels, lower than about 1 cm, even when the subsidence for 4 yrs reaches 140 cm. Therefore, the following constraint can be added to the inversion:

$$\phi_k^l = a_t^l(t_k - t_1) + b_t^l(t_k - t_1)^2 + e^l B_\perp^k + c_t^l \tag{6}$$

where $e^l B_\perp^k$ denotes the phase due to DEM error correlated with the perpendicular baseline of each acquisition, $B_\perp^k$. We then solve by least square inversion the system $\boldsymbol{d}^{\mathbf{c}} = \mathbf{G}^{\mathbf{c}}\mathbf{m}^{\mathbf{c}}$.

$$\begin{bmatrix} d_1^l \\ \vdots \\ d_k^l \\ \vdots \\ d_{N_l}^l \\ 0 \\ \vdots \\ 0 \end{bmatrix} = \begin{bmatrix} \begin{bmatrix} \\ & G_l & \\ \\ \end{bmatrix} & \begin{bmatrix} 0 & 0 & 0 & 0 \\ \vdots & \vdots & \vdots & \vdots \\ 0 & 0 & 0 & 0 \end{bmatrix} \\ \gamma \cdot \begin{bmatrix} 0 & \cdots & 0 & \cdots & 0 \\ 1 & \ddots & & & \vdots \\ \vdots & \ddots & 0 & & 0 \\ \vdots & & \ddots & \ddots & \vdots \\ 1 & \cdots & \cdots & 1 & 0 \end{bmatrix} & \begin{bmatrix} 0 & 0 & -B_\perp^1 & -1 \\ -(t_2-t_1) & -(t_2-t_1)^2 & -B_\perp^2 & -1 \\ \vdots & \vdots & \vdots & \vdots \\ \vdots & \vdots & \vdots & \vdots \\ -(t_{M_l}-t_1) & -(t_{M_l}-t_1)^2 & -B_\perp^{M_l} & -1 \end{bmatrix} \end{bmatrix} \begin{bmatrix} m_1^l \\ \vdots \\ m_{M_l}^l \\ a_t^l \\ b_t^l \\ e^l \\ c_t^l \end{bmatrix}$$

The weight, γ, scaling the additional matrix, is sufficiently small to insure that: a) if $\mathbf{G}_l^{\mathbf{T}}\mathbf{G}_l$ is invertible the increments m_k^l are not affected by the additional constraint (Eq. (6)), b) if not, the additional constraint only sets the relative delays between independent image groups. In all cases, a_t, b_t and e are the best fit coefficients to all parts of cumulated phase delays that are constrained by the interferometric data set. The use of Eq. (6) allows to strongly reduce the artifacts associated with the singularity of $\mathbf{G}_l^{\mathbf{T}}\mathbf{G}_l$, provided that Eq. (6) models most of the phase delay signal. The average subsidence rate or velocity is then obtained by a linear fit of $(\phi_k^l - e^l B_\perp^k)$. The noise that was present in the original velocity map after SVD inversion has now disappeared.

In the following, to study the temporal evolution of the displacement, we will focus on the points without missing links.

4.2. Results

Fig. 12 shows the average velocity map of the subsidence with a ground resolution of 30×30 m superimposed on a radar backscatter amplitude map. The largest displacement rates are located in Nezahualcoyotl and Chalco (about 38 cm/yr). In the main deformation areas, the correlation coefficient between displacement and time is always close to ~0.99, showing an almost perfect linear temporal behavior.

In the areas surrounding the alluvial deposits and on the volcanoes, the correlation coefficients are significantly negative, suggesting that these areas slightly uplift with respect to transition zone, at the borders of the main subsidence zone concentrated on the lacustrine deposits. The far field InSAR delays are not well defined enough to assess whether this relative uplift corresponds to a regional rebound due to water unloading in the aquifer or whether a slight subsidence rate should be added to all velocity values, therefore extending the subsidence area away from its main limits contoured by the lacustrine deposits. Fig. 13 shows the map of the DEM error, proportional to the coefficient, e^l, superimposed on a radar backscatter amplitude image. Negative DEM errors occur mainly in the lacustrine areas where subsidence takes place. On the volcanoes flanks, DEM errors show short scale "ondulations" aligned with the DEM hydrographic structures.

On Fig. 14, we display a few examples of time series corrected for the DEM errors contribution ($e^l B_\perp$). Note that the chosen points have no ($\mathbf{G}_l^{\mathbf{T}}\mathbf{G}_l$) rank deficiencies. Fig. 14 a_1 shows a point subsiding mostly linearly at 15 cm/yr in the radar LOS. A close look allows to see a progressive subsidence acceleration. This can be clearly seen in Fig. 14a_2 where the differences between the time series and the linear regression are plotted and fitted with a quadratic fit. Fig. 14b_1–b_2 shows a similar behavior, with a subsidence rate of 17.6 cm/yr in the radar LOS, but with a subsidence deceleration. On Fig. 14c_1–c_2, the point subsiding at 34.8 cm/yr in the radar LOS presents only a very slight subsidence deceleration. Finally, the same point, after removal of the quadratic temporal behavior, presents a small positive correlation between phase delay and $B_\perp$ corresponding to a DEM error of 1.4 m (Fig. 14d_1–d_2). The residuals around the fitted curves in panels a_2, b_2, c_2, and d_2, constrain the amplitude of the propagation delay not explained by Eq. (6). It corresponds to noise, turbulent atmospheric patterns, and other possible temporal trends in displacement. Residuals are in general in the range [−1, +1] cm. Examples shown on Fig. 14a, b and c, are cases well representative of the

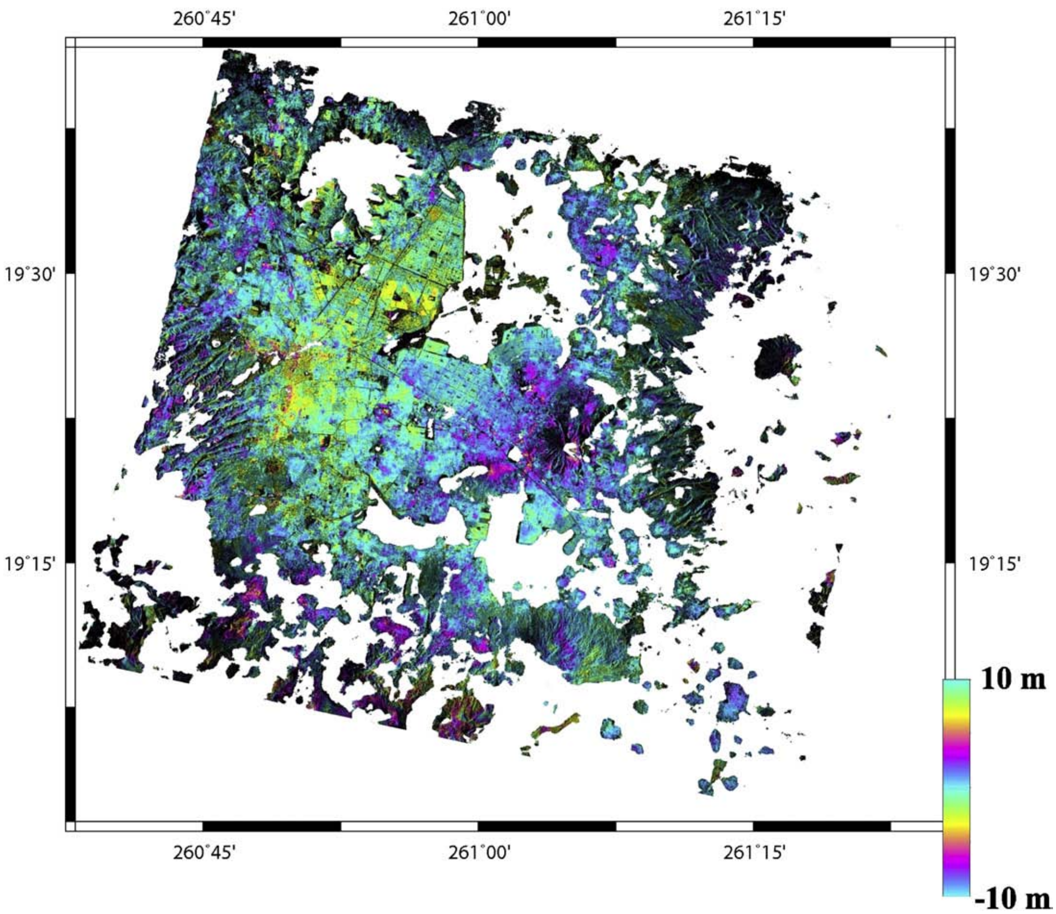

Fig. 13. DEM errors derived from the estimated slope, e^l, of the phase variation with $B_\perp$, superimposed on a radar backscatter amplitude map.

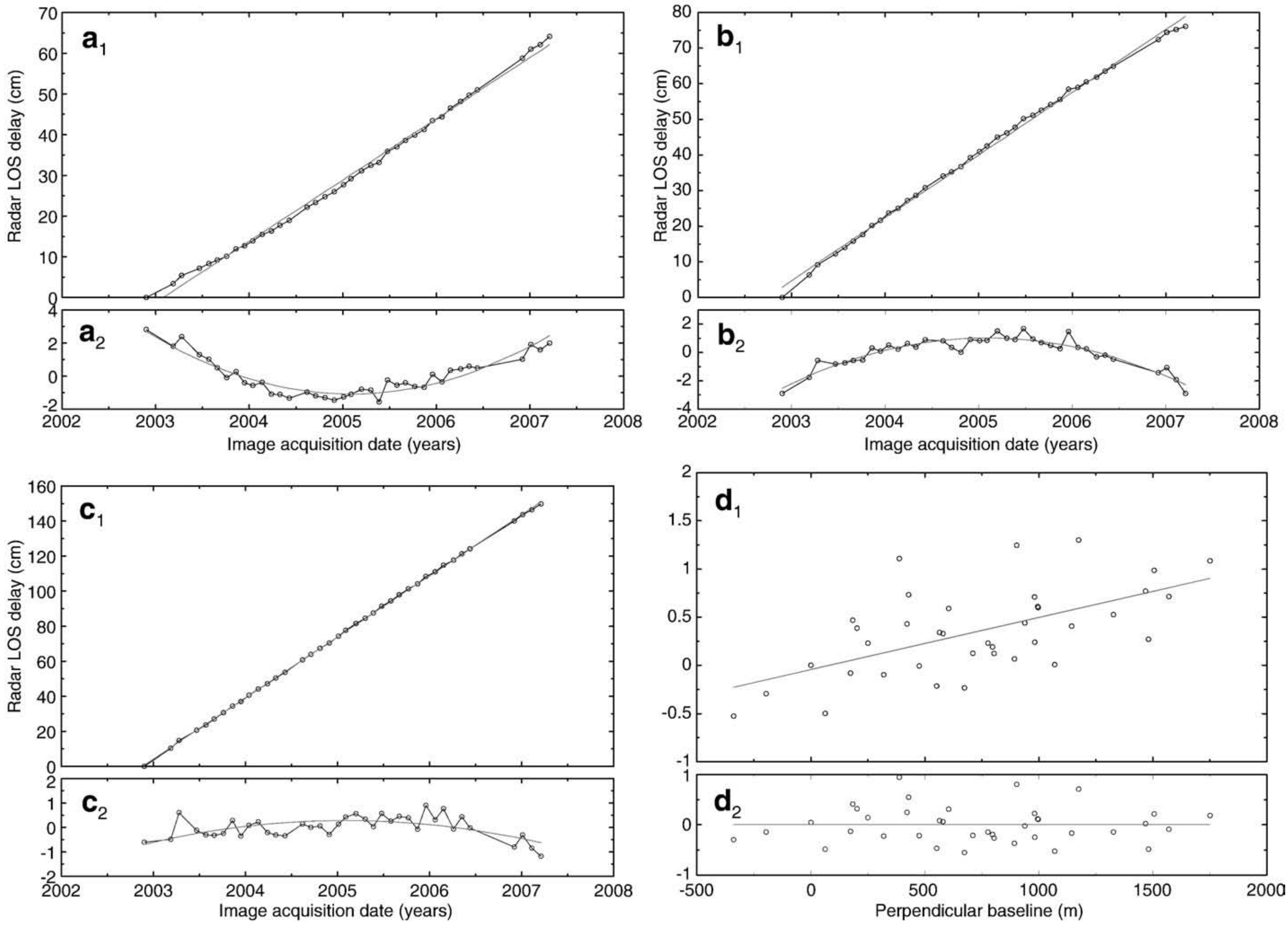

Fig. 14. a_1) Example of a subsidence time series showing acceleration, gray line: linear fit. a_2) Residuals between the linear fit and data points, fitted with a quadratic polynomial (gray line), expressing acceleration. b_1) Example of subsidence time series showing a deceleration. Gray line: linear fit. b_2) Residuals between the linear fit and data points, fitted with a quadratic polynomial (gray line), expressing deceleration. c_1) Example of subsidence time series showing an almost constant subsidence rate (gray line: linear fit). c_2) Residuals between the linear fit and data. The quadratic line (gray) shows a tenuous subsidence deceleration. d_1) Example of a small DEM error contribution varying with $B_\perp$, gray line: linear fit with slope e^l. d_2) Residuals between the linear fit and $B_\perp$. Note: In panels (a_1–c_2), the DEM error contribution has been estimated and removed. In panels (d_1) and (d_2), the quadratic temporal behavior has been estimated and removed.

evolution of the Mexico City subsidence over the whole metropolitan area. However, a few areas, with limited spatial extent, present significative pluriannual variations. No seasonal signal can be identified (if it exists, its amplitude is clearly below the noise amplitude).

The error, σ_{slope} ~ 0.06 cm/yr, on the average subsidence rate is estimated from the standard deviation of the residual, σ_{res} ~ 0.4 cm, and from the standard deviation of the date distribution, σ_{date} ~ 1.17 yr, as: $\sigma_{\mathrm{slope}} = \frac{1}{\sqrt{N_{\mathrm{image}} - 3}} \frac{\sigma_{\mathrm{res}}}{\sigma_{\mathrm{date}}}$.

4.3. Comparison with GPS measurements

The subsidence rates measured by a few GPS stations located in the Mexico City area (Cabral-Cano et al., 2006) can be compared with InSAR derived subsidence rates at the same locations. Permanent GPS stations MRRA, MPAA and MOCS placed near the metro stations, Rio de los Remedios, Pantitlan and Oceania, respectively, work since about 2005. The UPEC permanent GPS station located in the downtown area is operated since 2004, and the UIGF GPS permanent station, placed at the UNAM University, records data since 1997. The AIBJ campaign point located in the airport area has been measured during 10 twenty-four hour sessions, at the end of the dry season, between 1995 and 2001 (Cabral-Cano et al., 2006). The InSAR slopes at GPS points location result from a linear regression of the displacement time series from the end of 2002 to the beginning of 2007. Table 1 shows the comparison between GPS (from Cabral-Cano et al., 2006) and InSAR mean velocity (cm/yr) on each site, together with their estimated uncertainties. Both measurements are in overall in good agreement, however the differences reach up to 2.3 cm/yr, well below given error bars. The InSAR measurements at these GPS points correspond to low $\phi_{\mathrm{RMS_{pixel}}}$ values, that guarantees the measure quality, and to low lateral variability (except for MOCS station located on the flank of a hill). The differences between GPS and InSAR rates may correspond to the measure characteristics: punctual for GPS and with some spatial

Table 1
Subsidence rates (cm/yr) measured at the GPS stations (Cabral-Cano et al., 2006) and comparison with the InSAR derived subsidence rates.

Point	GPS	InSAR
UIGF	~0	0.06 ± 0.05
AIBJ	29.1	28.00 ± 0.04
MRRA	25.6 ± 0.5	27.75 ± 0.06
MPAA	21.2 ± 0.2	23.59 ± 0.06
UPEC	8.4 ± 0.6	8.95 ± 0.06
MOCS	16.9 ± 0.3	16.18 ± 0.05

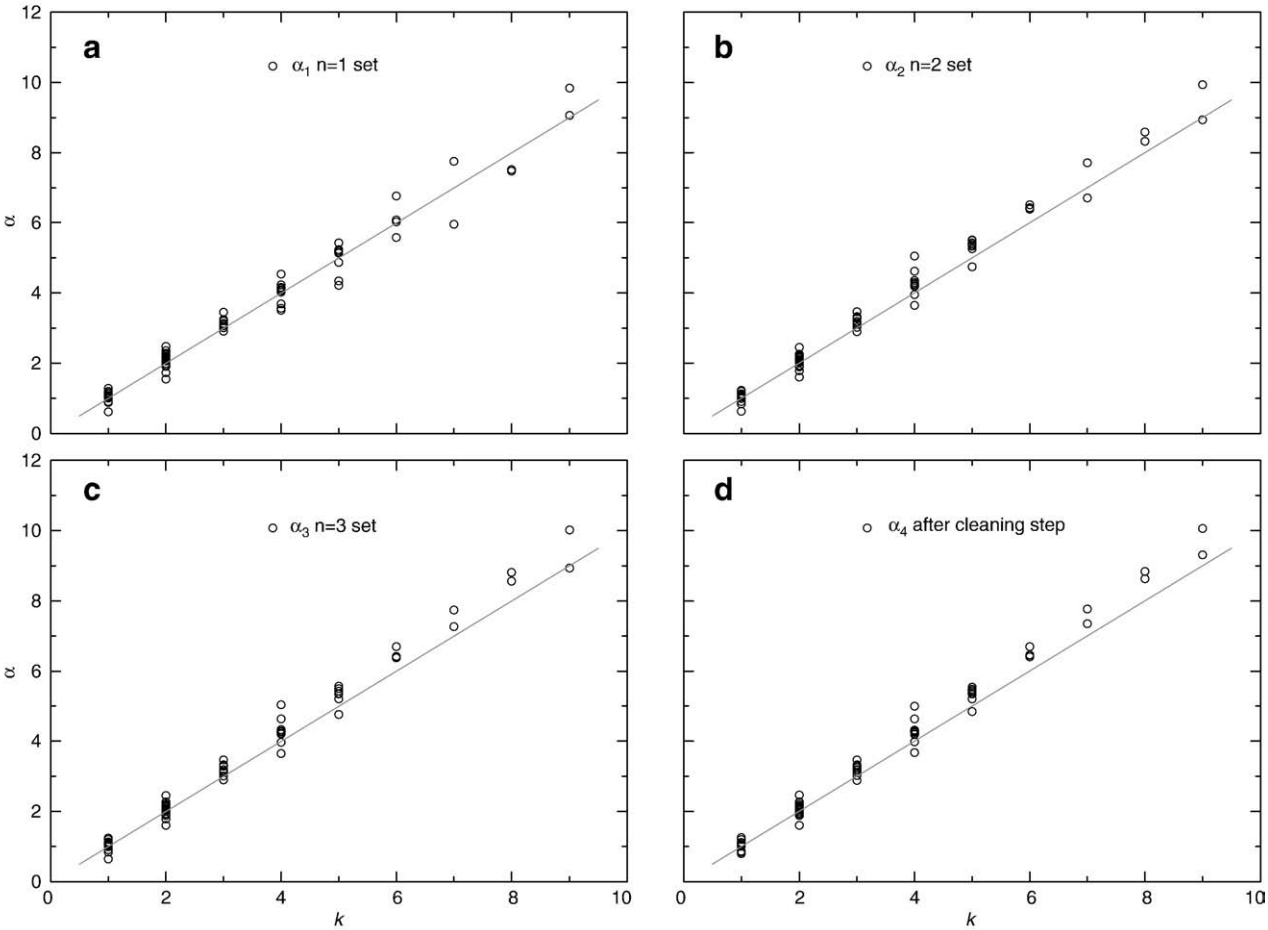

Fig. 15. (a–d) Scaling factor, α, calculated between each interferogram and the stack (displayed in Fig. 6) for the interferogram sets ($n=1$, $n=2$, $n=3$ and after cleaning step) produced by the unwrapping method. The solid gray lines shows the expected value of α_n, $\alpha_n = k$, for interferograms performed with a temporal baseline equal to $k \times 35$ days. This prediction should be verified if the subsidence varies linearly with time.

filtering (over ~100 m) for InSAR. A further study is however necessary to explain the GPS/InSAR discrepancies.

5. Conclusions

In this paper, we derive a method to help interferogram unwrapping that is the main obstacle towards analyzing the Mexico City subsidence by InSAR. The method principle is to reduce the number of fringes to unwrap by removing from the original interferogram the stratified atmospheric contribution and a scaled interferogram stack, which represents a part of the deformation spatial pattern. The residual interferogram is unwrapped by SNAPHU after applying a low-pass filter whose effect is restituted afterwards. The method described in this paper is iterative. We analyze unwrapping errors at each iteration step by checking the closure of the redundant interferometric system. This is a useful tool to detect where unwrapping errors are located and which interferogram they affect. However this tool is only used for diagnosis.

Both this method and the checking of the internal consistency of the interferogram network could be applied in other areas to the ground motion quantification by InSAR, provided that the spatial shape of the deformation is relatively stable through time (with possible amplitude fluctuations). This might often be the case for deformation led by potentiometric variations in aquifer or by mining activity.

Moreover, we present an inversion method of small baseline interferogram network, differing from classical SVD decomposition and that is best suited to the Mexico City data configuration. It is applied over pixels where critical interferometric links are missing. It is particularly useful when separated groups of images do not overlap in time along the perpendicular baseline axis. Such a situation should be common when strong temporal and geometrical decorrelation occurs. The inversion method can be applied to other areas, if the ground motion is mostly linear with time, or elsewhere using constraints adapted to other types of temporal behavior.

Both developed methods allow us to generate an accurate subsidence velocity map over the Mexico City Metropolitan area. It has a 30 m × 30 m resolution, little noise and a precision of the order of ~0.6 mm/yr. The accuracy is better than that obtained by the five interferograms stack (~5 cm/yr). The velocity map should be useful for new urban constructions, damage prevention, restoration and straightening of key urban structures affected by subsidence. It is especially important in areas of abrupt transitions between lacustrine sediments and volcanic rocks, i. e., where large subsidence gradients occur.

Our work also provides deformation time series from the end of 2002 to the beginning of 2007 with a 30 m × 30 m resolution. Although they reflect the almost perfectly linear temporal behavior of the subsidence in the lacustrine area, we detect areas where subsidence velocity is gradually increasing and others where it is decreasing. This should bring constraints on the aquitard compaction phenomenon, the water pore pressure evolution in the clay layer and possible non linear clay consolidation properties.

Furthermore, we show that the transition area around the lacustrine basin appears to uplift very slowly with respect to the lacustrine basin borders. This implies either a slight compaction of the aquifer itself (and not only the clay sediments in the aquitard) or a general rebound of the Mexico Basin due to water unloading. In any case, a better definition of the far field ground displacement is required in order to determine the absolute motion in the transition zone, and thus understand its nature.

Acknowledgments

We would like to thank the European Space Agency (ESA) for supplying the ENVISAT images through the category 1 project no. 3979. We thank the Mexico National Science and Technology Council (CONACyT) for its financial support. This work has also been supported by the French National Research Agency under the grant ANR-2007-MDCO-04, www.efidir.fr. We also thank the two anonymous reviewers and the Special Issue Editors whose comments improved the manuscript.

Appendix A

A.1. Iteration steps

We describe here in detail the iteration steps that lead to the formation of three sets of interferograms: the first set ($n=1$) is unwrapped by ROI_PAC (see Section 2.1), ϕ^1_{unw}, and the second ($n=2$) and third ($n=3$) sets are the results of two iterations based on SNAPHU (Chen and Zebker, 2000).

a) Formation of the second set of unwrapped interferograms, $n=2$.
   1) The parameter estimation from ϕ^1_{unw} using Eq. (4) is not always accurate at this stage due to the presence of some unwrapping errors in ϕ^1_{unw}, and because the branch-cut unwrapping algorithm proceeds only in part of the scene, i.e., in the areas across which the phase can be continuously described. This leads to an estimate of the twisted plane (a_1, b_1, c_1, d_1) and of atmospheric contribution β_1 prone to errors and, to a lesser extent, to inaccuracies in the stack scaling factor, α_1.
   2) At this first stage, the residual interferogram $e^{i\phi^1_{\mathrm{res}}}$ is only computed as $e^{i\phi^1_{\mathrm{res}}} = e^{i(\phi_{\mathrm{raw}} - \alpha_1\phi_{\mathrm{stack}})}$. Note that it is important to remove the stack scaled version from the wrapped raw differential interferogram, $e^{i\phi_{\mathrm{raw}}}$, due to very large displacement gradients possibly close to aliasing, that can be attenuated or destroyed by filtering. The adaptive filtering is best applied afterwards on the residual interferogram $e^{i\phi^1_{\mathrm{res}}}$.
   3) Unwrapping proceeds on the residual interferogram using the procedure described in Appendix A.2. SNAPHU allows to unwrap all patches of disconnected but coherent areas. This is only possible because $e^{i\phi^1_{\mathrm{res}}}$ has now a limited number of fringes and after applying an additional low-pass filter.
   4) The new unwrapped phase, $\phi^2_{\mathrm{unw}} = \phi^{1_{\mathrm{unw}}}_{\mathrm{res}} + \alpha_1\phi_{\mathrm{stack}}$, presents fewer unwrapping errors than ϕ^1_{unw}. In particular, unwrapping errors across the narrow subsiding corridor (see Figs. 6, 8e and f) linking the two main subsiding zones disappear. Moreover, it allows to recover information in the far field.

b) Formation of the third set of unwrapped interferograms, $n=3$.
   1) The parameters in Eq. (4) are now estimated from ϕ^2_{unw}. As ϕ^2_{unw} is also unwrapped in the far field, where high volcanoes are located, the residual orbit errors (a_2, b_2, c_2, d_2) and tropostatic delays (β_2) are better defined with less tradeoff than in the first iteration step. The latter, combined with the removal of most unwrapping errors, allows us to obtain a better estimation of the stack scaling factor, α_2.
   2) The residual interferogram is thus computed from the raw differential interferogram and from parameters α_2 and β_2:

$$e^{i\phi^2_{\mathrm{res}}} = e^{i(\phi_{\mathrm{raw}} - \alpha_2\phi_{\mathrm{stack}} - \beta_2 z)}$$

   3) As in (a) (3).
   4) The new unwrapped interferogram phase, ϕ^3_{unw}, obtained by $\phi^3_{\mathrm{unw}} = \phi^{2_{\mathrm{unw}}}_{\mathrm{res}} + \alpha_2\phi_{\mathrm{stack}} + \beta_2 z$, presents less unwrapping errors than ϕ^2_{unw}.

Finally, the parameters of Eq. (4) are re-estimated to build the interferograms corrected from residual orbital error and tropostatic contribution yielding a new stack scaling factor, α_3. On Fig. 15, we compare the estimated values of α_1, α_2 and α_3 to those expected if the subsidence is linear with time. The values of α slightly changes with the iteration and are always close to the “linear” expectation with some deviations that may be due to atmospheric patterns or to non linear deformation events.

A.2. Unwrapping of the residual phase

The following steps performed to unwrap the residual phase are displayed in Fig. 9 in a case example.

a) We first apply the ROI_PAC nonlinear adaptive spatial filtering to the residual interferogram $e^{i\phi_{\mathrm{res}}}$ (see Fig. 9c) to obtain $e^{i\phi^{\mathrm{adf}}_{\mathrm{res}}}$.
b) The residual interferogram is further low-pass filtered by computing the average complex in adaptive sliding windows, $e^{i\phi^{lp}_{\mathrm{res}}}$, (Fig. 9d). We apply this strong low-pass filter to run the SNAPHU unwrapping algorithm in a reasonable computer time and to partly fill non coherent areas with interpolated phase values before unwrapping disconnected patches.
c) The low-pass filtered interferogram, $e^{i\phi^{\mathrm{lp}}_{\mathrm{res}}}$, is unwrapped using SNAPHU yielding $\phi^{\mathrm{lp_{unw}}}_{\mathrm{res}}$ (Fig. 9e).
d) We assume that the phase of $e^{i(\phi^{\mathrm{adf}}_{\mathrm{res}} - \phi^{\mathrm{lp}}_{\mathrm{res}})}$ is within the range $[-\pi, \pi]$ and add it back to $\phi^{\mathrm{lp_{unw}}}_{\mathrm{res}}$ leading to the final unwrapped residual phase, $\phi^{\mathrm{adf_{unw}}}_{\mathrm{res}}$ (Fig. 9f). We also mask areas that remain noisy after adaptive filtering (these areas can be seen on Fig. 9c and compared with mask on Fig. 9f).

References

Beauducel, F., Briole, P., Froger, J.L., 2000. Volcano-wide fringes in ERS synthetic aperture radar interferograms of Etna (1992–1998) — deformation or tropospheric effect? Journal of Geophysical Research 105 (B7), 16,391–16,402.
Berardino, P., Fornaro, G., Lanari, R., Santosti, E., 2002. A new algorithm for surface deformation monitoring based on small baseline differential SAR interferograms. IEEE Transactions on Geoscience and Remote Sensing 40 (11).
Cabral-Cano, E., Dixon, T.H., Miralles-Whilhelm, F., Sanchez-Zamora, O., Diaz Molina, O., Carande, R.E., 2006. Space geodetic imaging of rapid ground subsidence in Mexico City. Geological Society of America Bulletin. doi:10.1130/B26001.1.
Carrera-Hernández, J.J., Gaskin, S.J., 2007. The Basin of Mexico aquifer system: regional groundwater level dynamics and database development. Hydrogeology Journal 15 (8), 1577–1590.
Cavalié, O., Doin, M.P., Lasserre, C., Briole, P., 2007. Ground motion measurement in the Lake Mead area, Nevada, by differential synthetic aperture radar interferometry time series analysis: Probing the lithosphere rheological structure. Journal of Geophysical Research 112, B03403. doi:10.1029/2006JB004344.
Chaabane, F., Avallone, A., Tupin, F., Briole, P., Maitre, H., 2007. A multitemporal method for correction of tropospheric effects in differential SAR interferometry: application to the Gulf of Corinth Earthquake. IEEE Transactions on Geoscience and Remote Sensing 45 (6), 1605–1615.
Chen, C.W., Zebker, H.A., 2000. Network approaches to two-dimensional phase unwrapping: intractability and two new algorithms. Journal of the Optical Society of America A 17, 401–414.
Delacourt, C., Briole, P., Achache, J., 1998. Trophospheric corrections of SAR interferograms with strong topography. Application to Etna. Geophysical Research Letters 25 (15), 2849–2852.
Farr, T.G., Kobrick, M., 2000. Shuttle Radar Topography Mission produces a wealth of data. American Geophysical Union EOS 81, 583–585.
Ferretti, A., Prati, C., Rocca, F., 2000. Nonlinear subsidence rate estimation using permanent scatterers in differential SAR interferometry. IEEE Transactions on Geoscience and Remote Sensing 38 (5).
Ferretti, A., Prati, C., Rocca, F., 2001. Permanent scatterers in SAR interferometry. IEEE Transactions on Geoscience and Remote Sensing 39 (1).
Goldstein, R.M., Werner, C.L., 1998. Radar interferogram filtering for geophysical applications. Geophysical Research Letters 25 (21), 4035–4038.
Goldstein, R.M., Zebker Howard, A., Werner Charles, L., 1988. Satellite radar interferometry — two-dimensional phase unwrapping. Radio Science (ISSN: 0048-6604) 23, 713–720 (July–Aug.).
Hanssen, R.F., 2001. Radar Interferometry: Data Interpretation and Error Analysis. Kluwer Academic Publishers. 308 pp.
Hooper, A., Zebker, H.A., 2007. Phase unwrapping in three dimensions with application to InSAR time series. Journal of the Optical Society of America. A 24, 2737–2747.
Hooper, A., Zebker, H., Segall, P., Kampes, B., 2004. A new method for measuring deformation on volcanoes and other natural terrains using InSAR persistent scatterers. Geophysical Research Letters 31, L23611. doi:10.1029/2004GL021737.

Pinel, V., Hooper, A., De la Cruz-Reyna, S., Reyes-Davila, G., Doin, M.P., 2007. Study of the deformation field of two active Mexican stratovolcanoes (Popocatepetl and Colima Volcano) by time series of InSAR data. Proceedings FRINGE Workshop, ESA Special Publication SP-649.

Puysségur, B., Michel, R., Avouac, J.P., 2007. Tropospheric phase delay in InSAR estimated from meteorological model and multispectral imagery. Journal of Geophysical Research 111 (B12), 7166–7174.

Rosen, P.A., Hensley, S., Peltzer, G., Simons, M., 2004. Updated repeat orbit interferometry package released. EOS Transactions - American Geophysical Union 85 (5).

Santoyo, E., Ovando-Shelley, E., Mooser, F., y León, E., 2005. Síntesis Geotécnica de la Cuenca del Valle de México, Editorial TGC, Mexico.

Scharroo, R., Visser, P.N.A.M., Mets, G.J., 1998. Precise orbit determination and gravity field improvement for the ERS satellites. Journal of Geophysical Research 103 (C4), 8113–8127.

Schmidt, D.A., Bürgmann, R., 2003. Time-dependent land uplift and subsidence in the Santa Clara valley, California, from a large interferometric Synthetic Aperture Radar data set. Journal of Geophysical Research 108 (B9).

Strozzi, T., Wegmuller, U., Werner, C., Wiesmann, A., Spreckels, V., 2003. JERS SAR Interferometry for Land Subsidence Monitoring. IEEE Transactions on Geoscience and Remote Sensing 41 (7).

Tortajada, C., 2006. Water management in Mexico City metropolitan area. Water Resources Development 22 (2), 353–376.

Usai, S., 2003. A least squares database approach for SAR interferometric data. IEEE Transactions on Geoscience and Remote Sensing 41 (4).

Wadge, G., et al., 2002. Atmospheric models, GPS and InSAR measurements of the tropospheric water vapour field over Mount Etna. Geophysical Research Letters 29 (19), 1905. doi:10.1029/2002GL015159.

Yun, S.H., Zebker, H., Segall, P., Hooper, A., Poland, M., 2007. Interferogram formation in the presence of complex and large deformation. Geophysical Research Letters 34, L12305.